Author: Uitert, Edo van
Title: Weak gravitational lensing in the red-sequence cluster survey 2
Date: 2012-05-29

2
Data reduction of the RCS2

In this chapter we present the weak lensing analysis of the Red Sequence Cluster Survey 2 (RCS2). The shape catalogues that result from this analysis are used in all science chapters of this thesis. We begin with a description of the survey specifications, then discuss the reduction steps, and detail the creation of the shape catalogues. Finally, we describe a number of basic tests we have performed to ensure the robustness of the results.

2.1 Introduction

The rise of weak gravitational lensing studies has been closely related to the ability to accurately measure the shapes of large numbers of galaxies. With the advent of mosaic CCD cameras that imaged several square degrees of sky, the conditions were set to extract the lensing signal from the data and use it for science. From the first detection of the lensing signal by Tyson et al. (1990), the field has rapidly expanded and has proven to be of great use in a wide variety of research areas, ranging from the study of galaxy formation and evolution using galaxy-galaxy lensing, to the testing of cosmological models through the measurement of the lensing properties of the large scale structure (LSS). One of the main propellants of the rapid progress of the field has been the continuous inauguration of ever larger cameras and telescopes with larger fields of view and improved image quality, and the resulting mapping of ever larger parts of the sky to greater depths. As a result, the number of galaxies whose shapes has been reliably determined has increased by orders of magnitudes (from a few thousands to tens of millions in the most recent surveys), and so has the signal-to-noise of the lensing measurements.

To date, a broad variety of imaging surveys has been used for lensing. We show in Table 2.1 a list of the most recent surveys and their main characteristics relevant for weak lensing studies. In any survey, the observation time can either be used to image a large patch of sky, but shallow, or to image a small area to great depths. The weak lensing science that can be extracted strongly depends on this choice. The wide but shallow surveys (e.g. SDSS) contain many objects at low redshift, and the stacked lensing signal of low-redshift lenses (galaxies, galaxy groups and/or clusters) provides tight constraints on the distribution of matter in the nearby universe (e.g. Mandelbaum et al. 2006; Sheldon et al. 2009). In addition, these surveys are particularly suited for studying the lensing signal of low-mass galaxies (as there are many of them), and for studies of the

Table 2.1: The characteristics of current large imaging surveys relevant for weak lensing studies

Survey (1)	Size (2)	Depth (3)	Bands (4)	PSF size (5)
SDSS	10 000	22	$ug\boldsymbol{r}iz$	1.5
RCS2	900	24.3	$g'\boldsymbol{r'}(i')z'$	0.7
CFHTLS-WIDE	171	24.8	$u^*g'r'\boldsymbol{i'}z'$	0.7
RCS1	90	25.2	$\boldsymbol{R_c}z'$	0.8
CTIO	90	23.5	$\boldsymbol{R}$	1.05
CFHT12K-VIRMOS	17	24.5	BVR**I**	0.75
COSMOS	1.64	28.6	$\boldsymbol{I}g$	0.09

(1) name of the survey; (2) area of the survey [deg^2]; (3) depth of the band used for lensing (note that different definitions have been utilized); (4) wavelength coverage (PI imaging, the lensing band in bold font); (5) median size of the PSF in the band used for lensing [arcsec].

intrinsic alignment of galaxies (e.g. Hirata et al. 2004), which can occur if the galaxies are subject to the same large-scale gravitational field, e.g. during their time of formation. Finally, if the PSF[1] is small, these surveys can be used for constraining cosmological parameters (Amara & Réfrégier 2007). The galaxies in a small but deep survey (e.g. COSMOS) are spread over a large range of redshifts, which makes those surveys particularly suited for evolutionary studies, e.g. to study how the stellar mass-to-halo mass relation evolves (Leauthaud et al. 2012) or how the universe expands (Schrabback et al. 2010). For deep surveys it is also possible to measure the lensing signal from individual massive low-redshift clusters (e.g. Okabe et al. 2010).

With a size of 900 deg^2 and a depth of 24.3 in the r'-band, the RCS2 fills the gap between these two survey strategy extremes of width and depth. The survey was specifically designed to optimize the detection of clusters from $z \sim 0.1$ to 1 via the red sequence method (Gladders & Yee 2000), a technique that takes advantage of the fact that the early-type galaxies belonging to a given cluster have very similar colours, and their positions are clustered. The main goals of the survey are to use the cluster catalogue to constrain the cosmological parameters Ω_M and σ_8, to study the evolution of clusters, to define a large sample of strong lensing clusters and to perform weak lensing studies. Thanks to its combination of size, depth and seeing, the RCS2 is well suited for a large range of lensing studies, as we demonstrate in this thesis.

In this chapter, we will discuss the characteristics of the RCS2 in Section 2.2. The reduction we have performed is described in Section 2.3. In Section

[1]The Point Spread Function (PSF) describes the observed shape of a point source (e.g. a star) across the field-of-view of the camera. The shape and size of the PSF are mainly determined by the optics of the telescope and the conditions in the atmosphere. The observed galaxies in an image have been convolved with the PSF, and their shapes need to be corrected for this convolution before they can be used in lensing studies. If the PSF is small and round, this correction is generally more accurate, which is crucial for lensing studies that rely on the correlation of galaxy ellipticities.

2.4 we detail the creation of the shape catalogues. We have performed some basic tests to ensure that no errors occurred in the reduction process that, if unnoticed, could affect our science results. This is presented in Section 2.5. Note that various details of the survey have already been described in Gilbank et al. (2011) and van Uitert et al. (2011). This chapter is intended to provide more details on the steps carried out to construct the catalogues with shape measurements. In particular, the various quality checks discussed in Section 2.5 have not been described in these papers.

2.2 Red Sequence Cluster Survey 2

The RCS2 is a nearly 900 square degree multicolour imaging survey, carried out with the Canada-France-Hawaii Telescope (CFHT), a 3.6m telescope located at the top of Mauna Kea, Hawaii. With a median seeing of $0.7''$ in the r'-band, this site is exceptionally suited for deep surveys that require a good resolution. The camera that has been used is the wide field imager MegaCam (Boulade et al. 2003), which consists of 36 2048×4612 pixel CCD chips, placed in 4 rows and 9 columns. The lay-out of the chips, and the variation of the pixel size across the sky, are shown in Figure 2.1. The pixel size variation is the result of small non-linearities in the camera optics. MegaCam covers about 1×1 degree on the sky, properly sampling the PSF with an average pixel size of $0.186''$. The size of the camera enables the surveying of large parts of the sky in a reasonable amount of time.

The survey consists of two parts: the primary survey, which covers about 740 square degrees, is divided into 13 well-separated patches on the sky (including the uncompleted patch 1303), each with an area ranging from 20 to 100 square degrees. The second part is formed by the CFHT Legacy Survey Wide, comprising of 171 square degrees of imaging data in $u^{\star}$, g', r', i' and z'. In this thesis we have only used data from the primary survey area. If references are made to 'the survey' from here on, we implicitly mean the primary survey. The location of the various patches on the sky are shown in Figure 2.2. The lay-out of the exposures within the patch CDE2338 is shown in Figure 2.3 as an example. A number of these patches coincide with other surveys, including the Sloan Digital Sky Survey (SDSS) (York et al. 2000) and the WiggleZ Dark Energy Survey (Blake et al. 2008). Combining data from these surveys is advantageous, as it enables science projects that cannot be performed on either of the data sets individually, as we demonstrate in Chapters 3 and 4.

The observations of the survey were performed in three filters (g', r' and z'). About half of the survey area is observed in the i'-band as part of the Canada-France High-z quasar survey (Willott et al. 2005), and was made available for the RCS2 through a data exchange agreement. Details of the observations in each of these bands can be found in Table 2.2. Note that the depth of the r'- and z'-band were chosen to detect $M^* + 1$ red-sequence cluster galaxies at a redshift $z \sim 1$.

The survey is observed in single exposures, since the observations are deep enough for the survey objectives, and valuable CCD read-out time is saved (≈2 minutes per read-out). As a result, small gaps in the surveyed area are present due to the separation between the chips, but they cause no limitations to the science projects. A disadvantage of single exposures is that the removal of cos-

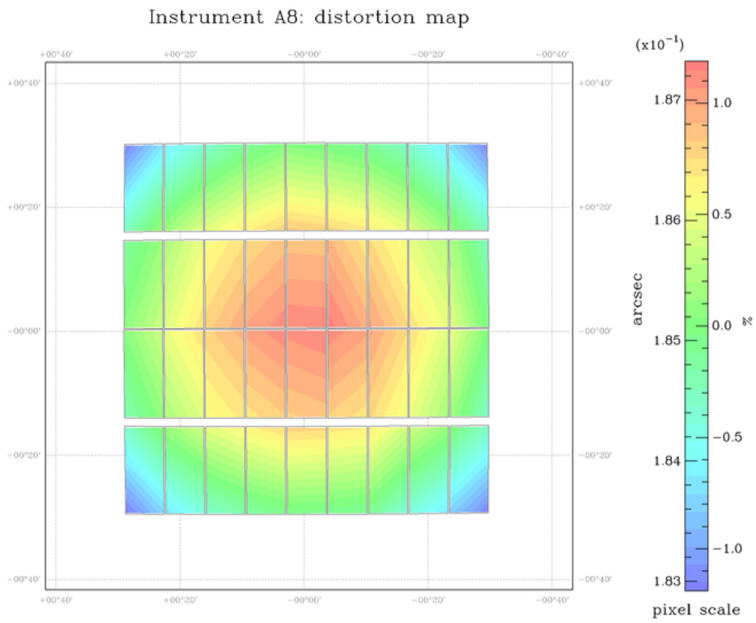

Figure 2.1: The variation of the pixel size in the MegaCam camera, also known as the camera distortion, induced by slight non-linearities in the camera optics. The colour bar indicates the size of the pixels in arcsec, and their relative size with respect to the mean. The pixel size is largest in the centre of the camera. The lay-out of the individual chips is clearly discernible. The variation is smooth and constant over time; the small jumps in the pattern between the central chips are caused by a lack of stars to trace the relative astrometry. The camera distortion generates a false shear signal, which has been corrected for in the lensing analyses. This image is a product of the THELI pipeline (Erben et al. 2005, 2009).

mic rays is more difficult, especially those that hit galaxies and stars. However, they introduce no bias in the analyses, but only act as a minor source of noise.

To quantify the image quality, the variation of the PSF is measured across the field in each exposure. The images of the stars are used for this purpose because they are essentially point sources. For each star, the Full Width Half Maximum (FWHM) is determined, which is the distance from the star's centre where the flux reaches half of its maximum value. The median stellar FWHM is a measure of the quality of the PSF; the larger it is, the more the observed images of galaxies are smeared out, which causes them to appear rounder. Correcting the observed shapes for this smearing becomes increasingly difficult for larger PSF sizes, particularly for small and faint galaxies. Additionally, the depth of the images decreases if the PSF is large, as very faint galaxies are smeared out such that they become buried in the background noise. Weak lensing studies therefore require observations with small PSF sizes.

The median stellar FWHM of the primary survey images in each band is

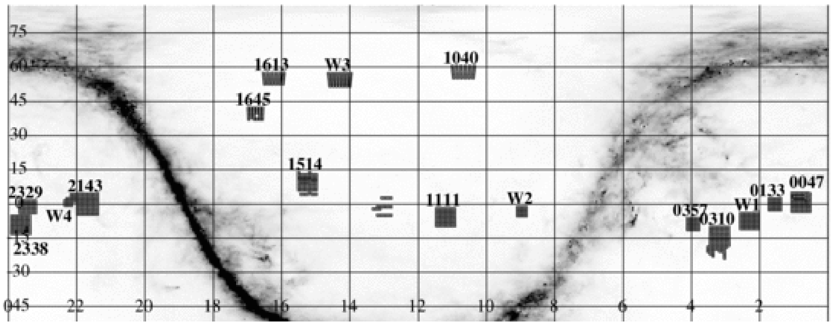

Figure 2.2: The location of the RCS2 patches on the sky in Cartesian projection, as a function of right ascension and declination. The grey scale denotes the dust maps from Schlegel et al. (1998). The labels indicate the name of the patches. The name-less patch in the centre is the uncompleted patch 1303, for which no photometric catalogues exist because of its non-contiguous nature (image courtesy: David Gilbank).

Table 2.2: Details on the various observing bands of the RCS2 (PI data)

Band	Area [deg^2]	t_{exp} [sec]	$m_{lim}$$^{(a)}$	Median seeing
g'	740	240	24.4	$0.79''$
r'	740	480	24.3	$0.71''$
i'	400	500	23.7	$0.53''$
z'	740	360	22.8	$0.67''$

(a) the 5σ point source limiting magnitude, averaged over all chips

given in Table 2.2. It differs between the observing bands due to the difference of the atmospheric conditions during the observations. The distribution of the FWHMs in the r'-band, the band used for the lensing analysis, is shown in Figure 2.4. The values of the FWHM range from $0.5''$ to $1.0''$, and have a median value of $0.71''$. This is exceptionally good for a ground-based survey (e.g. compare Table 2.1.)

In November 2004, when approximately 20% of the primary survey area had been observed, the lens L3 was accidentally mounted incorrectly after the wide-field corrector had been disassembled. This surprisingly led to a significant improvement in the PSF pattern, and the new configuration was kept. The dramatic improvement of the PSF pattern is demonstrated by plotting the stellar ellipticity vectors across the camera in Figure 2.5; prior to that moment, the PSF showed a strong pattern, with ellipticities reaching up to 15% in the corners of the images. After this moment, no clear PSF pattern could be discerned, and the amplitude of the PSF ellipticity was significantly reduced. The FWHM distribution of the two sets are shown in Figure 2.4. We note, however, that none of the area observed prior to November 2004 has been discarded, as we correct for the potential residual systematics that may result from the very elliptical PSF (detailed in Section 2.5.4).

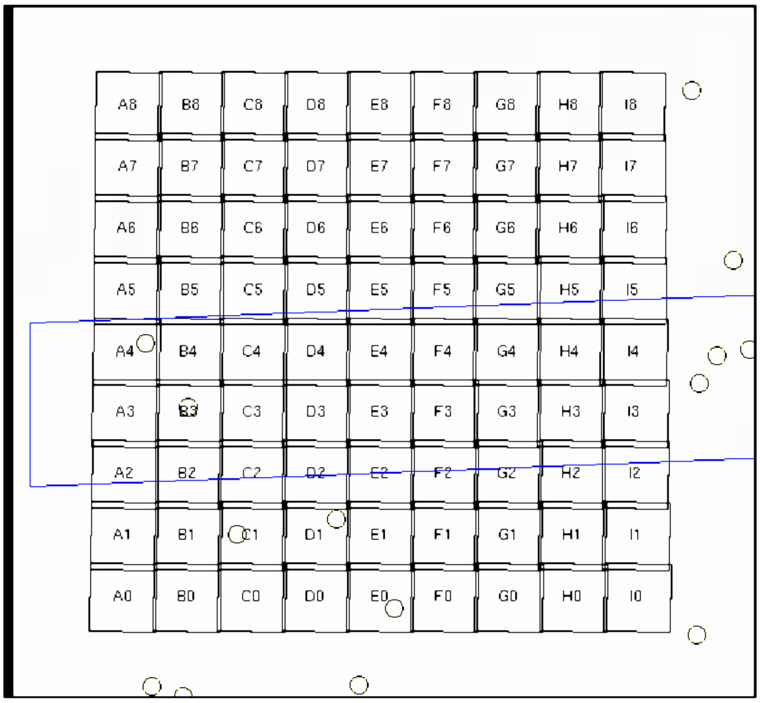

Figure 2.3: The location of the 81 exposures in the patch 2338, as a function of right ascension (horizontal axis) and declination (vertical axis). The circles denote the location of bright stars from the Bright Star Catalogue 4, with a magnitude between 4 and 6. The blue box shows the overlap with the SDSS (image courtesy: rcs2.org)

2.3 Data reduction

The basic reduction of the images is performed with Elixir[2] at the CFHT. Elixir consists of a collection of programs that is used for the instant assessment of the image quality of telescope data, and also contains programs to perform the basic image reduction. The goal of this reduction is to remove the instrumental signature from the data, so that the images can be used for science. This reduction corrects for the positive offset of the detector of the camera, for the dark current (the electrons that are occasionally released in the CCD due to thermal motions instead of photons), for the unequal sensitivity of the pixels in the CCD, and for the presence of fringes, which are caused by thin-film interference effects in the detector. Once this basic reduction has been performed, objects are detected with `SExtractor` (Bertin & Arnouts 1996). The locations of the detections are compared to the USNO 1.0 star catalogue to calculate the astrometric solution, such that the (x, y)-locations of the pixels can be translated into sky coordinates. Finally, by comparing the observed photon counts of these stars to their known magnitudes, zero points, that is the conversion factor between counts and apparent magnitude, are calculated for each image.

[2]http://www.cfht.hawaii.edu/Instruments/Elixir/

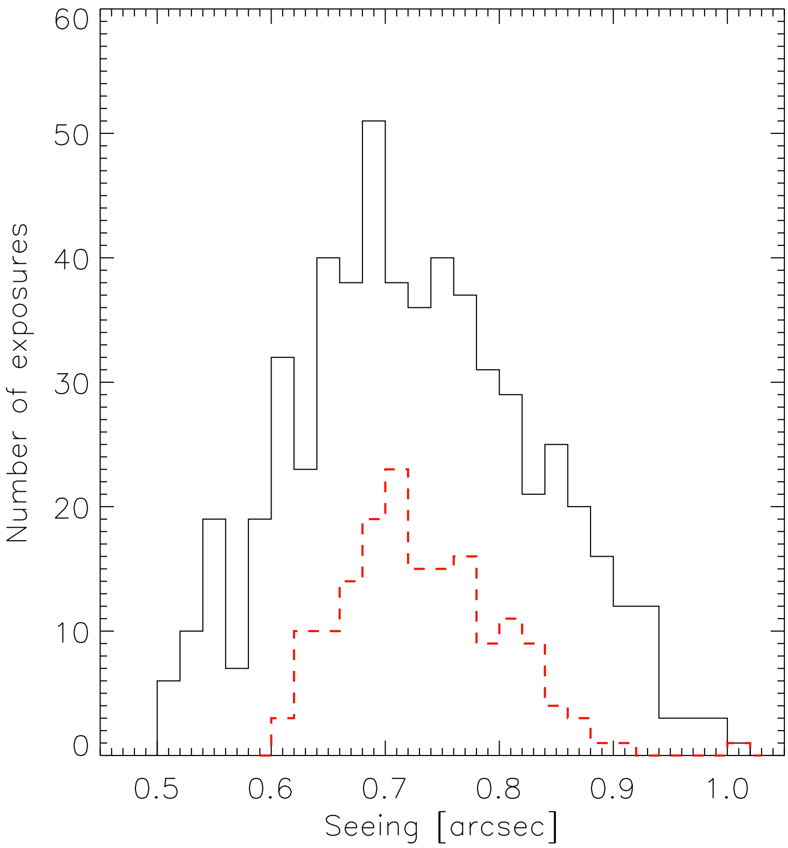

Figure 2.4: The distribution of the FWHM of the stars in the 739 r'-band images in the primary survey area of the RCS2. The solid black (dashed red) line shows the distribution for the images observed after (before) the change of the lens configuration.

Using the zero points, we can determine the apparent magnitudes of all detected objects in the image.

We retrieve the Elixir processed images from the Canadian Astronomy Data Centre (CADC) archive[3]. We use the THELI pipeline (Erben et al. 2005, 2009) to subtract the image backgrounds, create weight maps that we use in the object detection phase, and to identify satellite and asteroid trails. To obtain a more accurate astrometric solution, we run `SCAMP` (Bertin 2006) on the images, which enables us to match our catalogues to other catalogues, including the photometric catalogues from Gilbank et al. (2011), and the spectroscopic catalogues from the SDSS. Additionally, we use the polynomial coefficients from `SCAMP` that describe the mapping from image to sky coordinates to calculate the systematic shear that results from the camera distortion, and for which we have to correct.

[3]http://www1.cadc-ccda.hia-iha.nrc-cnrc.gc.ca/cadc/

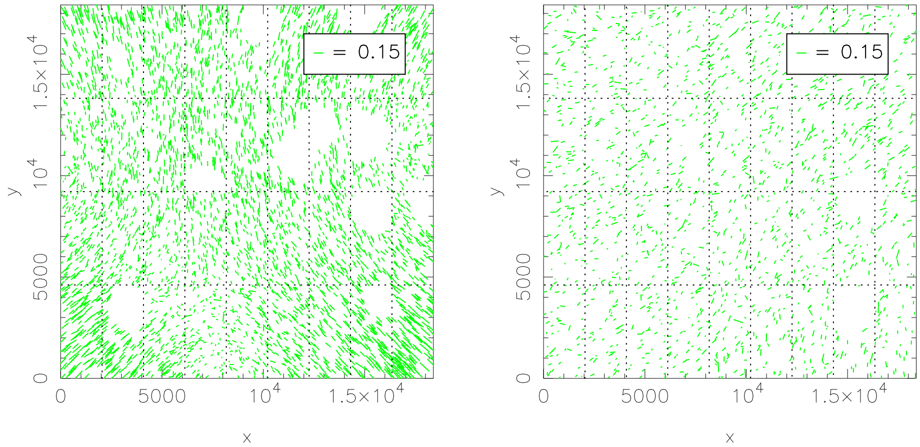

Figure 2.5: The ellipticities of the stars in two exposures as a function of position in the mosaic. The green sticks indicate the size and orientation of the ellipticities of the stars that are used for modeling the PSF (note that only half of the total number of stars is plotted for clarity). The dashed lines approximately denote the chip boundaries. On the left-hand side, we show the stellar ellipticities in the field 2143H6, which was observed before the lens configuration changed. The PSF shows a clear pattern, and is very elliptical in the corners of the image. On the right-hand side, we show the stellar ellipticities in 1613A2, which was observed after the lens-configuration change. No pattern is observed in the PSF, and the PSF ellipticity is small across the image.

Each exposure contains areas where the photometry is affected by the reflection haloes of large stars, diffraction spikes, satellite and asteroid trails, and other anomalies. Excluding such areas in lensing studies is important, as the shape measurement of galaxies in those areas is unreliable, and may contaminate the lensing signal. For that purpose, we create image masks for our lensing analyses by combining the masks from the automated masking routines from THELI with the RCS2 masks, as neither of these masks individually works sufficiently well for our purposes. The THELI mask poorly covers the large stellar reflections, potentially because we run the pipeline on individual chips. The RCS2 masks covers these large stellar reflections well, but misses many satellite and asteroid trails that are properly masked by THELI. To exclude the contaminated areas that are not covered by either mask, we inspect all masks by eye, and manually improve them where necessary.

An additional advantage of the visual inspection of the data was the discovery of various problematic exposures that were not flagged by the standard image quality checks. Two sets of these exposures are discussed in the last two paragraphs of the next section.

2.3.1 Problematic exposures

For a number of exposures, problems occurred either during the observations or the image reduction. Consequently, some images had to be excluded from the science analysis. We describe the problems of these fields below.

During parts of the observing run 05BQ03, the upper half of the camera (chips 18 to 36) was not read out due to a failure in the power supply in the South controller. The four RCS2 r'-band images that were taken in this run have been discarded.

The read-out of chip 5 failed for the twenty-one r'-band exposures taken in observing runs 03BQ06 and 03BQ07. This did not affect the other chips, and the exposures were included.

The r'-band exposures of the patches 0047F8, 2338I1 and 2338I8 exhibit a strange feature; faint horizontal and vertical trails emerge from the bright stars, which are most likely caused by an electronic problem during the read-out. As it is not clear how this anomaly depends on the brightness, nor whether stars and galaxies are affected in an equivalent way, these three exposures have been removed from the science analyses.

Finally, the central pixels of the bright stars in chip 28 to 36 in the observing runs 04BQ02 and 04BQ03 have negative values. This problem was caused by a failure of the video board in the South controller, which resulted in the amplifier saturating at 32K instead of the usual 65K. All the problematic stars are masked, as to make sure they are not used to model the PSF. The exposures have been included in the science analyses.

2.4 Catalogue creation

We use `SExtractor` (Bertin & Arnouts 1996) to detect the objects in the images. From the object catalogues we select the stars, which are used for modeling the PSF variation across the images. An accurate model of the local size and shape of the PSF is essential, as the measured galaxy images have to be corrected for the smearing of the PSF to obtain their unconvolved shapes. Hence we require a clean star catalogue, that contains many stars distributed over the entire image in order to sample the spatial variation of the PSF. To separate the stars from the galaxies, we first identify the locus of the stellar branch in a size-magnitude diagram. We select the non-saturated objects close to the stellar branch with a S/N ratio larger than 30 and with no `SExtractor` flags raised. To remove small galaxies that have been misidentified as stars, and stars that have been affected by cosmic rays, we fit a second-order polynomial to both the size and the ellipticity of these star-candidates as a function of their position in the chip, and discard all 3-sigma outliers. We clean the stellar selection even further in the shape measurement pipeline by removing shape parameter outliers. All objects larger than 1.2 times the local size of the PSF are classified as galaxies, and passed on to the shape measurement pipeline. Smaller objects are not included as they consist of a mixture of stars and galaxies. The resulting effective galaxy number density is 11.6 arcmin^{-2}. Two diagnostic plots of the star-galaxy separation are shown in Figure 2.6. The separation has been fully automated, but as a precaution we inspect the diagnostic plots for all exposures by eye. The separation fails only for a few chips that have either very few stars or a PSF with a large FWHM, and we manually adjust those. As neighbouring patches overlap by ~ 1 arcminute, we remove all galaxies within 35 arcseconds from the image edges in order to avoid duplicating the objects in our analysis.

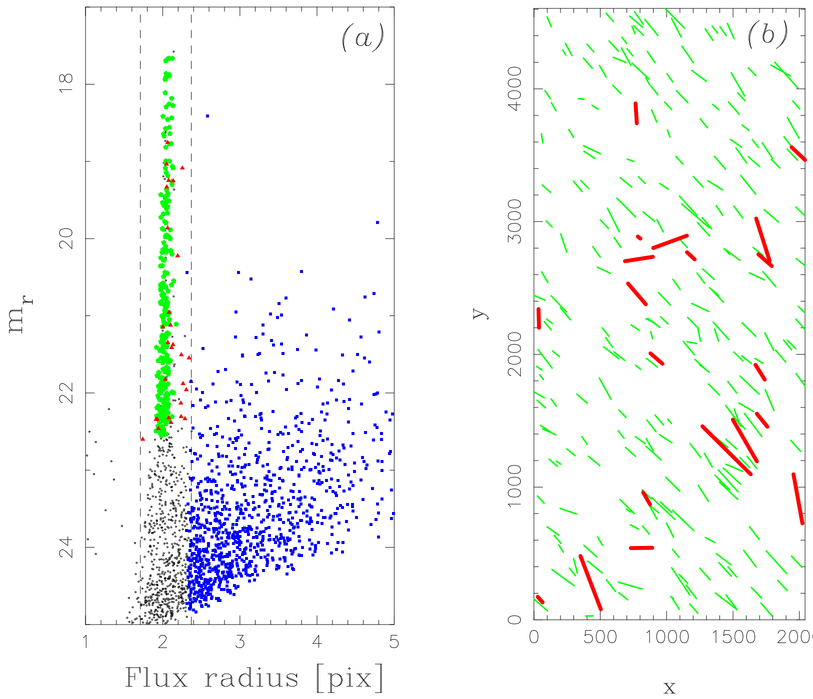

Figure 2.6: In panel (a), we show the size-magnitude diagram of one of the chips in a randomly picked exposure. The black dots are the `SExtractor` detections, the green pentagons are the selected stars, the red triangles are the 3-sigma outliers, and the blue squares are the selected galaxies. The dashed lines indicate the location of the stellar branch. Thanks to the good image quality the stars are easily separated from the galaxies. In panel (b), we show the location of the same stars and their ellipticity vectors as a function of position in the chip. The 3-sigma outliers are indicated by the thick red lines.

Elixir provides approximate zero-points for each pointing, which we use to measure the r'-band apparent magnitudes of the objects in the images. We correct the magnitudes for galactic extinction using the dust maps from Schlegel et al. (1998). We asses the quality of the photometry in Section 2.5.

2.4.1 Weak lensing analysis

For our lensing analysis we measure the shapes of galaxies with the KSB method (Kaiser et al. 1995; Luppino & Kaiser 1997; Hoekstra et al. 1998), using the implementation described by Hoekstra et al. (1998, 2000). There are several alternative methods to measure shapes of galaxies. We use the KSB method because it measures the shapes of galaxies accurately in simulations (see Section 2.5), and because it has been extensively used and tested on real data. Finally, the method is fast.

In KSB, galaxy shapes are defined by the raw pseudo ellipticities, which we call polarizations from here on:

$$\epsilon_1 = \frac{Q_{11} - Q_{22}}{Q_{11} + Q_{22}}; \epsilon_2 = \frac{Q_{12}}{Q_{11} + Q_{22}}, \tag{2.1}$$

where Q_{ij} is the weighted moment of the brightness distribution $B(\mathbf{x})$:

$$Q_{ij} = \int d^2\mathbf{x}\, B(\mathbf{x}) W(x) x_i x_j, \tag{2.2}$$

with $W(x)$ a Gaussian weight function. The weight function and the integral are centered at the galaxy. To convert the measured galaxy polarizations into ellipticities, the polarizations have to be corrected for the circularization by the weight function, and for smearing by the PSF. These corrections are described by complex formula that can be found in the original papers. To correct for the PSF, we need to determine the smear susceptibility tensor, $P^{\mathrm{sm}\star}$, which describes how the PSF affects the galaxy polarizations. $P^{\mathrm{sm}\star}$ is estimated by the combination of various higher-order moments of the brightness distribution of the stars in a chip. The components of the tensor are interpolated at the location of the galaxies using a polynomial that is third-order in y and second-order in x (the length of the chip in the y-direction is more than twice the length in the x-direction), fitted to each chip separately.

The PSF correction has a limited accuracy in practice. One of the reasons is that in the KSB formalism, it is assumed that the brightness distribution of stars can be described by an isotropic profile convolved with a small anisotropic kernel. The PSF is generally more complicated which may lead to biases. To study the magnitude of these biases, this implementation of KSB has been tested on simulations with a variety of PSFs, which we will discuss in Section 2.5.2.

The ellipticities of the galaxies are also affected by slight non-linearities in the mapping between the sky coordinates and the CCD pixels in the camera, an effect which is called camera distortion. We calculate the shear induced by this distortion using the polynomial coefficients from `SCAMP` that describe how the image coordinates are mapped onto the sky coordinates. The camera shear of MegaCam is shown in Figure 2.7. The images of both the stars and the galaxies are sheared, with a value reaching 1.5% at the corners of the images. At large lens-source separations, where the gravitational lensing signal is small, the camera shear dominates the observed lensing signal. Hoekstra et al. (1998, 2000) demonstrate that the observed shear is the sum of the gravitational shear and the camera shear. We therefore simply subtract the camera shear from the observed ellipticities of the galaxies to correct for it, after correcting the galaxy shapes for smearing by the PSF.

In real data, there is always shear present to some level that is not produced by gravitational lensing (systematic shear), due to imperfect PSF corrections, biases in the shape measurement pipeline, the image masks and the survey layout. When we measure the mean lensing signal around galaxies or clusters of galaxies on small scales, these systematic contributions average out since we generally average over a large number of lens-source orientations. On larger scales, however, we cannot average over many orientations, because we perform the lensing analysis on single exposures. We do this because including source galaxies from neighbouring exposures to the analysis barely improves the lensing signal-to-noise on small scales, which is the regime we are interested in in

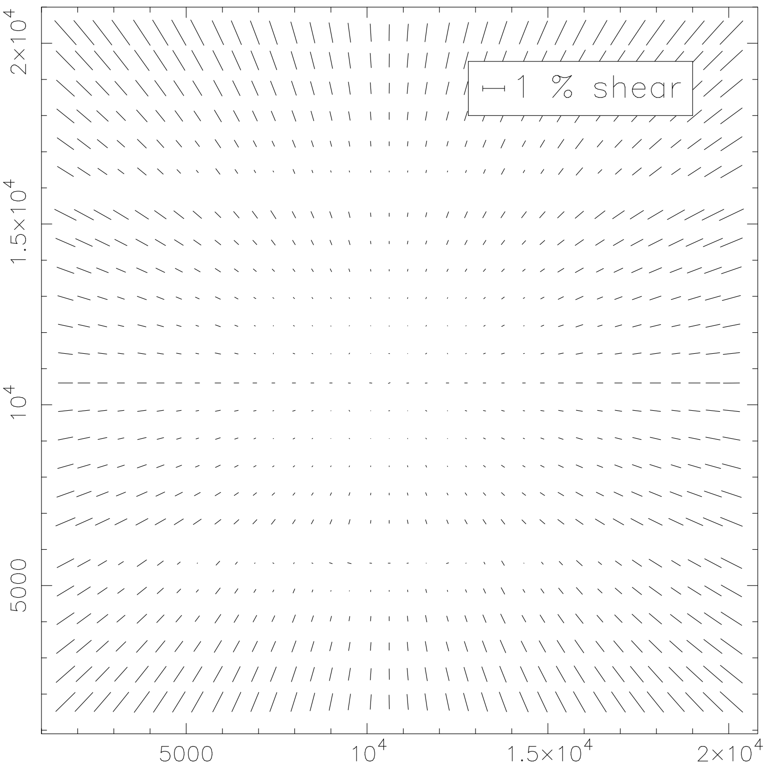

Figure 2.7: Shear induced by camera distortion in the MegaCam imager. The camera shear is largest in the corners of the mosaic, with values up to 1.5%. As the observed shear is the sum of the gravitational shear and the camera shear, we simply subtract the camera shear from the observed galaxy ellipticities to correct for it.

the studies of this thesis. Hence the source galaxies at large separations always reside in the corners. Consequently, there is systematic contribution to the real shear. To remove this signal, we measure the lensing signal around a catalogue of random lens positions. In the absence of systematic shear in the shape catalogues, the shear signal around random lenses is zero, but if systematic shear is present, the random signal and the real signal are equally affected. We use 40 000 random lenses per image, roughly 20 times the number of real lenses used at most per image in the science analyses. The random lensing signal is measured using the same binning, and subtracted from the real lensing signal. We test the correction in the next section.

2.5 Quality Checks

We perform various tests to assess the quality of the photometry and the shape measurements. Furthermore, we study the fidelity of our corrections for camera shear and systematic shear. These tests are done to ensure that no major systematics remain in the catalogues that may bias the science results.

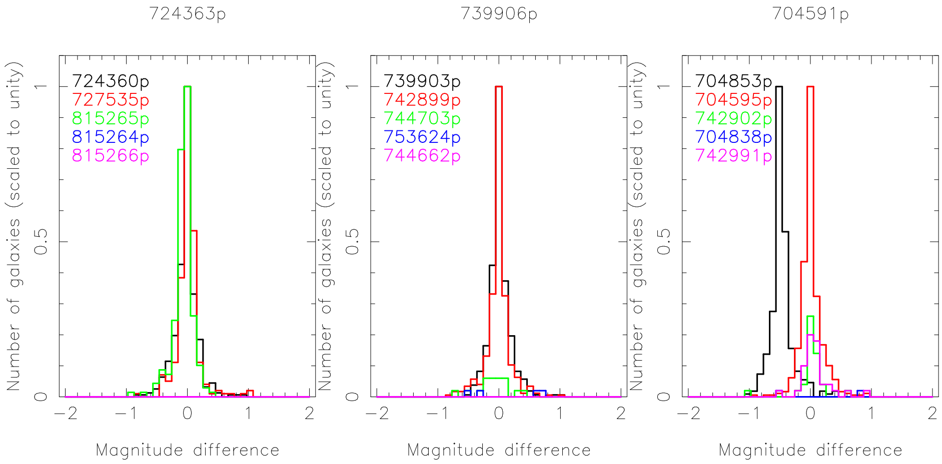

Figure 2.8: Internal comparison of the r'-band magnitudes of galaxies that reside in the areas that overlap with neighbouring exposures. Each overlapping exposure is indicated by a different colour, and their names shown in the top-left corners. The photometry of the majority of exposures agrees well internally, as the histograms are centered on zero and have a small width. Only a few exposures have erroneous zero-points. We show one example in the right-hand panel, where the zero-point of the image 704853 is off by ∼0.5 magnitude.

2.5.1 Photometry

As a check of internal consistency, we compare the magnitudes of the galaxies from different exposures that reside in the overlapping areas. Depending on its location in the patch, an exposure may overlap with up to 8 neighbours. We match the galaxies from adjacent fields, and make histograms of the difference in r'-band magnitudes. A few examples are shown in Figure 2.8. These histograms show that for nearly all exposures, the zero-points between neighbouring fields are consistent as the histograms are centered close to zero. Only for a few exposures, the histograms are significantly shifted from zero, which indicates that in either one of the exposures the zero-point is far off. As the exposures generally overlap with more than one neighbour, the fields with erroneous photometry are easily identified.

Next, we compare the 'raw' dust-corrected r'-band magnitudes of the galaxies to the more accurately calibrated ones from Gilbank et al. (2011). For each exposure we make a histogram of the difference in magnitudes. A few examples are shown in Figure 2.9. The histograms demonstrate that the magnitudes agree well for the majority of galaxies. The fields with an erroneous zero-point as revealed by the internal comparison are easily identified from these histograms as well since they are significantly shifted from 0. None of the histograms are Gaussian, but they all show a tail at $m_{r'} - m_{r',\mathrm{Gilbank}} < 0$. This is likely due to the fact that different apertures have been used in the measurements. In one exposure, the histograms are offset by $\Delta m_r \approx 2$, indicating that a major error occurred in one of the photometric solutions. On average, however, the magnitudes agree well, and differ in the r'-band by $\langle m_{r'} - m_{r',\mathrm{Gilbank}} \rangle = 0.00 \pm 0.26$. The scatter is dominated by faint galaxies; when we limit the comparison to

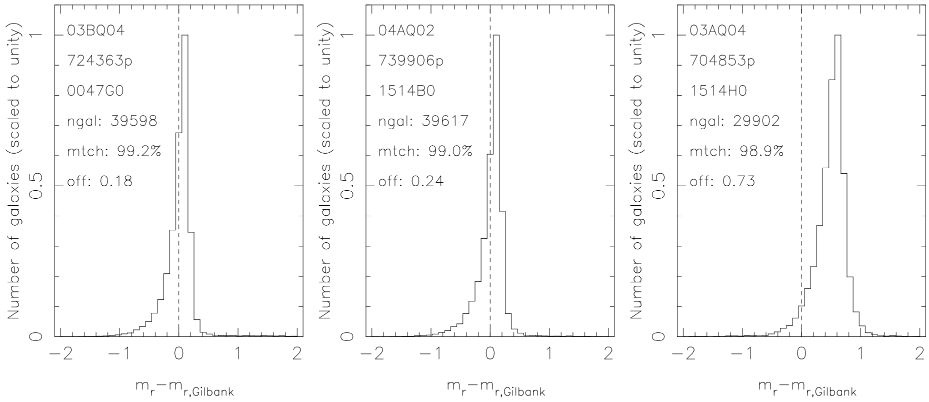

Figure 2.9: Comparison of the r'-band magnitudes of galaxies with the photometric catalogues from Gilbank et al. (2011) for three exposures. The left-hand and middle panel show the same exposures as in Figure 2.8, the right-hand panel shows the exposure with image number 704583 whose zero-point was found to be off, which is again confirmed. The top-left corner of each plot shows the observing run number, the image name, the patch name, the number of galaxies, the percentage of matched galaxies and the mean offset. For the majority of exposures, the magnitudes agree well. The non-Gaussian shapes of the histograms are likely due to a difference in the size of the aperture used for measuring the flux.

galaxies with $m_{r'} < 23$, we find $\langle m_{r'} - m_{r',\mathrm{Gilbank}} \rangle = 0.01 \pm 0.14$.

In the whole thesis we use the photometric catalogue from Gilbank et al. (2011), except in Chapter 3, as the photometric catalogue was not available at the time of writing. However, in Chapter 3 the 'raw' Elixir magnitudes are only used to select the source galaxy sample and for this purpose they are sufficiently accurate.

2.5.2 Galaxy shapes

The implementation of the KSB method we use has been tested on the Shear Testing Programme (STEP) simulations (the HH method in Heymans et al. 2006; Massey et al. 2007). The STEP simulations are used for the blind testing and comparison of shape measurement methods. These simulations consist of an artificial set of survey images, containing a large number of galaxies whose morphologies mimic those of real galaxies. To these galaxies a shear is applied which is constant, but differs from image to image. The images are then convolved with a variety of PSFs, to test the reliability of methods under different observing conditions. The goal of any of the tested methods is to determine as accurately as possible the value of the input shear. Its values is not known beforehand to avoid tweaking of the methods. The performance of each method is determined by two numbers, m_i and c_i, the multiplicative bias and the shear calibration bias, defined as

$$\langle \tilde{\gamma}_i \rangle - \gamma_i^{\mathrm{input}} = m_i \gamma_i^{\mathrm{input}} + c_i, \tag{2.3}$$

where i denotes the different components, $\gamma_i^{\mathrm{input}}$ is the input shear and $\langle\tilde{\gamma}_i\rangle$ is the averaged measured shear. A non-zero m_i indicates that the method does not respond one-to-one to shear, and a non-zero c_i generally indicates that the PSF has not been properly corrected for. For STEP1, the HH method has an average multiplicative bias of $\langle m\rangle = -0.015 \pm 0.006$, and a mean calibration bias $\langle c\rangle$ that is consistent with shot noise at the 0.1% level. For STEP2, the average $\langle m\rangle$ is -0.01, and the mean $\langle c\rangle$ is consistent with zero. Note, however, that for the simulations with a highly elliptical PSF (simulation set D and E in STEP2), all tested shape measurement pipelines (including the HH method) have a significant non-zero shear calibration bias. This is not a major concern in this thesis for a number of reasons. First of all, the area with a highly elliptical PSF in the RCS2 is very small compared to the total survey area; potentially biased galaxy shapes will not contribute much to the total signal. Furthermore, most of the systematics will average out since we measure the lensing signal around galaxies and galaxy clusters for a large number of random lens-source orientations. Finally, by subtracting the random lensing signal from the signal computed with real lenses, we remove PSF residuals from the galaxy-mass cross-correlation function at large-scales that are still present because we do not have enough lens-source orientations to average over. Note that in the measurement of the correlation between the ellipticities of galaxies, as is done in cosmic shear studies, or in cluster mass reconstruction studies, PSF residuals can introduce a significant bias in the result. The areas with a highly elliptical PSF should be excluded from such analyses. In conclusion, the results of the STEP simulations indicate that the HH method is a shape measurement method accurate and robust enough for the scientific purposes of this thesis, and suggest that the shear measured in the RCS2 data is underestimated by 1–2 % at most.

As for the photometry, we make an internal comparison of the ellipticity estimates using the galaxies in the areas that overlap with neighbouring exposures. Histograms of the differences in the e_2 ellipticity components are shown in Figure 2.10. The histograms are all centered on zero. Combining all the overlapping regions, we find that the average spread has a value 0.09, which decreases to 0.05 and 0.03 if we only compare galaxies with $m_{r'} < 23$ and $m_{r'} < 22$, respectively. The average galaxy polarization errors for these selections are 0.05, 0.02 and 0.01. The average *ellipticity* error of these galaxies is larger, however, due to uncertainties in the PSF correction. Additionally, we compare galaxies close to the sides of the image, where the PSFs pattern differs most between the images. Hence the values for the average spread are reasonable, which demonstrates that the method is stable, and the ellipticity estimate for a galaxy is robustly measured in the RCS2.

The shapes of galaxies in the RCS2 have been measured independently with the shapelet method (Refregier 2003; Refregier & Bacon 2003), using the implementation of Kuijken (2006). This shape measurement technique provides independent estimates of the ellipticity of galaxies. We compare the ellipticity components of 450 000 galaxies in Figure 2.11. For small ellipticities, the ellipticity components agree well. For galaxies with $e_i > 0.15$, the ellipticities measured with KSB are slightly larger than those measured with shapelets. This discrepancy might be caused by the rapid radial decline of the shapelets basis functions. Consequently, shapelets have difficulties in fitting galaxies with flat surface brightness profiles, and very elliptical galaxies, leading to biases in the ellipticity measurement.

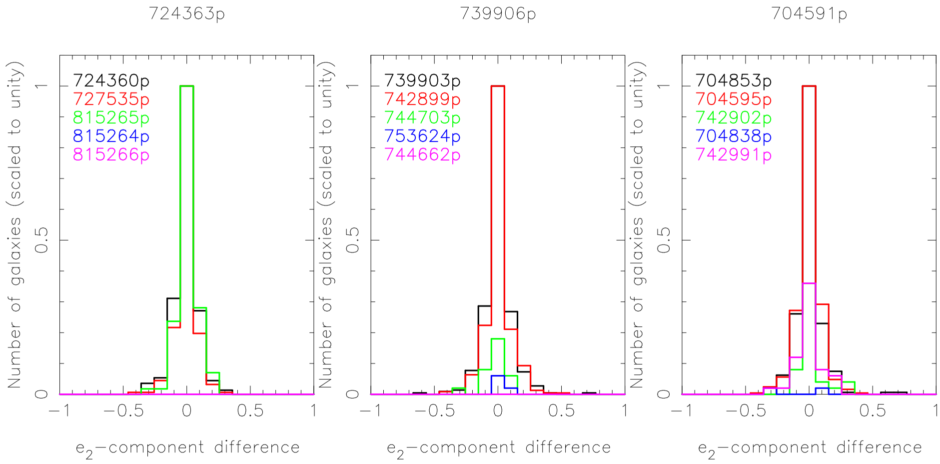

Figure 2.10: Three examples of the comparison of the e_2 ellipticity component of the galaxies that reside in the areas that overlap with neighbouring exposures. Each overlapping exposure is indicated by a different colour, and their names shown in the top-left corners. Both the e_1 and e_2 ellipticity component agree well internally, as all histograms are narrow and centered on zero. This demonstrates that the ellipticities of galaxies are robustly determined with the KSB method.

Another standard test performed in gravitational lensing is the measurement of the so-called cross shear. Gravitational lensing only produces 'tangential' distortions – the shapes of source galaxies are stretched in the direction perpendicular to the lens-source separation. The cross shear measures the shear component that is rotated by 45 degrees with respect to the lens-source separation vector. A non-zero cross shear indicates the presence of systematics in the shape catalogues. If the cross shear is zero, however, the shape catalogues are not necessarily free of systematics. The cross shear and the tangential shear are measured simultaneously in the science analyses. In all the lensing measurements we perform throughout this thesis, we find that the cross shear signal is consistent with zero. As an example, we refer the interested reader to Figure 3.5 in Chapter 3.

2.5.3 Camera shear correction

The camera shear results from slight non-linearities in the mapping between the sky coordinates and the CCD pixels. It is calculated by taking the gradient of the polynomial fits from `SCAMP` that describe the mapping between image to sky coordinates. The camera shear pattern is mainly radial, as can be seen in Figure 3.4 in Chapter 3. To check whether we properly remove the camera shear, we measure the tangential shear around the centre of the images, using the corrected and uncorrected galaxy ellipticities. The result of this test is shown in Figure 2.12. When we do not correct for camera shear, we observe that the measured signal turns negative towards the edges of the images. After the correction, the effect is reduced but some residual is still present. We attribute this to residual PSF systematics, as we demonstrate in the next section.

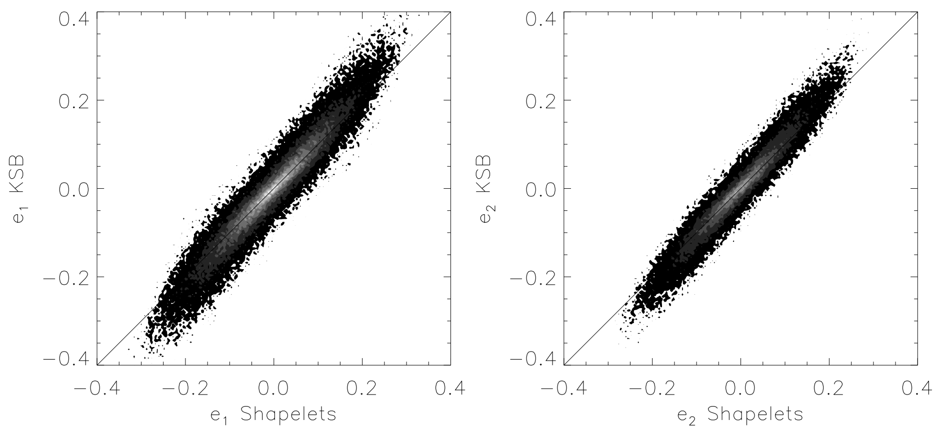

Figure 2.11: Comparison of the ellipticity components of 450 000 galaxies measured with the KSB method and with the shapelets method, for e_1 in the left-hand panel, and for e_2 in the right-hand panel. The ellipticities agree well for $e_i < 0.15$, but for larger ellipticities KSB measures larger values.

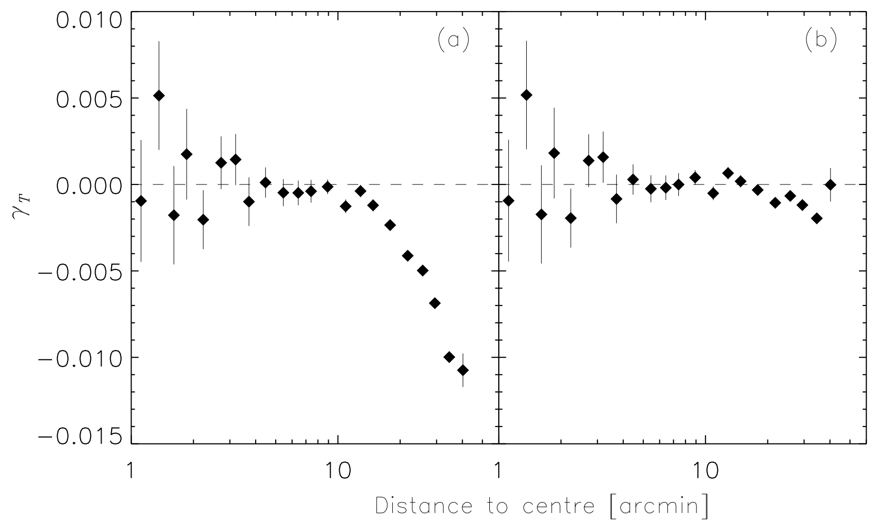

Figure 2.12: The shear around the centre of the camera. In panel (a), the correction for camera shear has not been applied. Consequently, the signal becomes negative at scales >10 arcmin as the camera distortion is mainly radial. We apply the camera shear correction in panel (b), which strongly suppresses the large-scale negative signal. A small residual negative signal is left, which is caused by imperfect PSF corrections of the galaxy shapes. In lensing measurements, the subtraction of the signal around random lenses corrects for this.

2.5.4 Random catalogues

For each image, a large number of random lens positions are generated. The lenses that reside inside the masked regions are removed. We measure

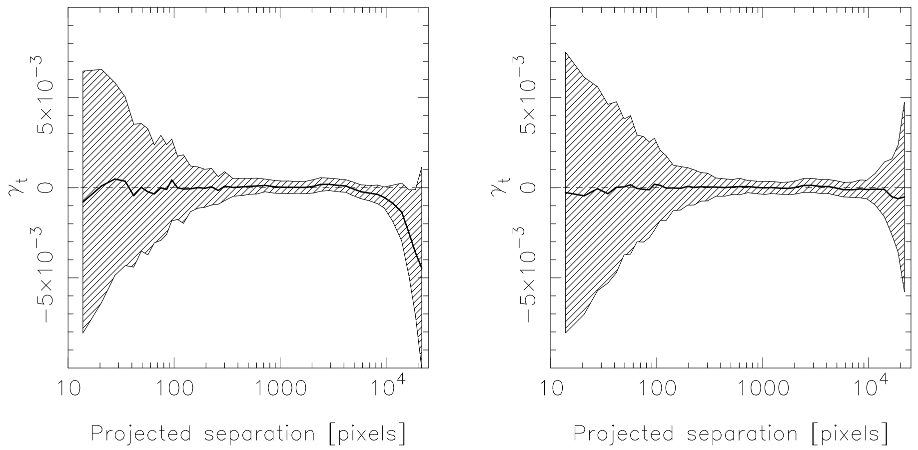

Figure 2.13: The signal of the random lens catalogues for the exposures taken prior to the lens-configuration change (left-hand panel), and the exposures observed afterwards (right-hand panel), after applying the correction for camera shear. The thick line shows the average, the hatched area shows the scatter between the exposures. The random signal of the left-hand panel turns negative at large scales, which indicate the presence of PSF residual systematics in the shape catalogues.

the lensing signal using 40 000 random lenses per image, and show the average signal in Figure 2.13 (after applying the correction for camera shear). The left panel shows the random signal for the 160 exposures taken prior to the change of the orientation of the lens, which took place in November 2004. The right panel shows the random signal for the 600 exposures taken after that moment. In both cases, the random signal on small scales is consistent with zero, since the signal is averaged over many lens-source orientations. At large scales, the random shear signal of the images observed before the lens configuration change turns negative. This residual pattern is due to imperfect PSF corrections of the galaxies that reside near the edges and corners of the images, where the PSF was found to be very elliptical (see Figure 2.5).

To demonstrate how the random signal impacts the lensing measurements, we measure the tangential shear around 1.6×10^6 lenses with magnitudes in the range $19.5 < m_{r'} < 21.5$, using 14×10^6 source galaxies with $22 < m_{r'} < 24$. We perform the measurement both with and without subtracting the random lensing signal, and show both results in Figure 2.14. Without correcting for the random signal, the shear increases from ∼6 to ∼10 arcminutes, after which it rapidly decreases and turns negative. Correcting the shear with the random signal removes this odd bump and negative signal. The corrected signal is smooth, suggesting that the correction for systematic contributions works well.

Bibliography

Amara, A. & Réfrégier, A. 2007, MNRAS, 381, 1018

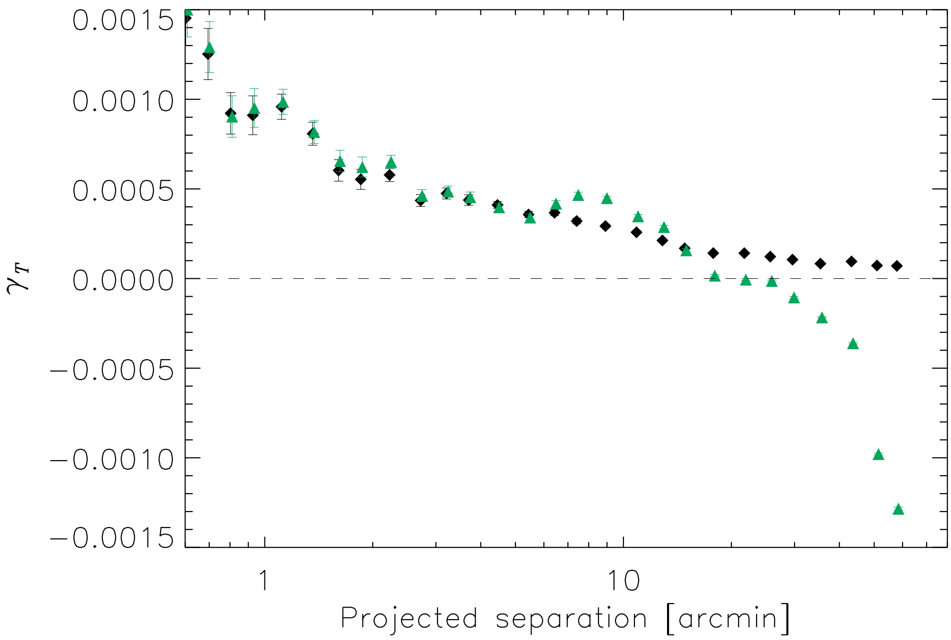

Figure 2.14: The stacked tangential shear around 1.6×10^6 magnitude-selected lenses ($19.5 < m_r < 21.5$) measured using 14×10^6 source galaxies with $22 < m_{r'} < 24$. The green triangles show the signal that has not been corrected for the random lensing signal, and is slightly negative at lens-source separations larger than 20 arcmin. Note that the effect is about ten times smaller than the camera shear. The black diamonds show the corrected signal, which is smoother at large scales and does not become negative. We did not use neighbouring exposures to measure the lensing signal in this figure, because this more clearly illustrates the main source of the systematic signal, i.e. imperfect PSF corrections in the corners of the images.

Bertin, E. 2006, in Astronomical Society of the Pacific Conference Series, Vol. 351, Astronomical Data Analysis Software and Systems XV, ed. C. Gabriel, C. Arviset, D. Ponz, & S. Enrique, 112

Bertin, E. & Arnouts, S. 1996, A&AS, 117, 393

Blake, C., Brough, S., Couch, W., et al. 2008, Astronomy and Geophysics, 49, 050000

Boulade, O., Charlot, X., Abbon, P., et al. 2003, in Society of Photo-Optical Instrumentation Engineers (SPIE) Conference Series, Vol. 4841, Society of Photo-Optical Instrumentation Engineers (SPIE) Conference Series, ed. M. Iye & A. F. M. Moorwood, 72–81

Erben, T., Hildebrandt, H., Lerchster, M., et al. 2009, A&A, 493, 1197

Erben, T., Schirmer, M., Dietrich, J. P., et al. 2005, Astronomische Nachrichten, 326, 432

Gilbank, D. G., Gladders, M. D., Yee, H. K. C., & Hsieh, B. C. 2011, AJ, 141, 94

Gladders, M. D. & Yee, H. K. C. 2000, AJ, 120, 2148

Heymans, C., Van Waerbeke, L., Bacon, D., et al. 2006, MNRAS, 368, 1323

Hirata, C. M., Mandelbaum, R., Seljak, U., et al. 2004, MNRAS, 353, 529
Hoekstra, H., Franx, M., & Kuijken, K. 2000, ApJ, 532, 88
Hoekstra, H., Franx, M., Kuijken, K., & Squires, G. 1998, ApJ, 504, 636
Kaiser, N., Squires, G., & Broadhurst, T. 1995, ApJ, 449, 460
Kuijken, K. 2006, A&A, 456, 827
Leauthaud, A., Tinker, J., Bundy, K., et al. 2012, ApJ, 744, 159
Luppino, G. A. & Kaiser, N. 1997, ApJ, 475, 20
Mandelbaum, R., Seljak, U., Kauffmann, G., Hirata, C. M., & Brinkmann, J. 2006, MNRAS, 368, 715
Massey, R., Heymans, C., Bergé, J., et al. 2007, MNRAS, 376, 13
Okabe, N., Takada, M., Umetsu, K., Futamase, T., & Smith, G. P. 2010, PASJ, 62, 811
Refregier, A. 2003, MNRAS, 338, 35
Refregier, A. & Bacon, D. 2003, MNRAS, 338, 48
Schlegel, D. J., Finkbeiner, D. P., & Davis, M. 1998, ApJ, 500, 525
Schrabback, T., Hartlap, J., Joachimi, B., et al. 2010, A&A, 516, A63
Sheldon, E. S., Johnston, D. E., Scranton, R., et al. 2009, ApJ, 703, 2217
Tyson, J. A., Wenk, R. A., & Valdes, F. 1990, ApJ, 349, L1
van Uitert, E., Hoekstra, H., Velander, M., et al. 2011, A&A, 534, A14
Willott, C. J., Delfosse, X., Forveille, T., Delorme, P., & Gwyn, S. D. J. 2005, ApJ, 633, 630
York, D. G., Adelman, J., Anderson, Jr., J. E., et al. 2000, AJ, 120, 1579